Title

Relating 18F-FDG image signal-to-noise ratio to time-of-flight noise-equivalent count rate in total-body PET using the uEXPLORER scanner

Journal

Physics in Medicine and Biology, 67(12)

ISSN

0031-9155

Authors

Leung, Edwin K

Abdelhafez, Yasser G

Berg, Eric

et al.

Publication Date

2022-06-21

DOI

10.1088/1361-6560/ac72f1

Peer reviewed

HHS Public Access

Author manuscript

Phys Med Biol. Author manuscript; available in PMC 2023 June 10.

Published in final edited form as:

Phys Med Biol. ; 67(12): . doi:10.1088/1361-6560/ac72f1.

Relating ^{18}F-FDG image signal-to-noise ratio to time-of-flight noise-equivalent count rate in total-body PET using the uEXPLORER scanner

Edwin K. Leung[1,2,3], **Yasser G. Abdelhafez**[1], **Eric Berg**[2], **Zhaoheng Xie**[2], **Xuezhu Zhang**[2], **Reimund Bayerlein**[1], **Benjamin Spencer**[2], **Elizabeth Li**[2], **Negar Omidvari**[2], **Aaron Selfridge**[1], **Simon R. Cherry**[2,1], **Jinyi Qi**[2], **Ramsey D. Badawi**[1,2]

[1]Department of Radiology, UC Davis Health, Sacramento, CA, United States

[2]Department of Biomedical Engineering, University of California, Davis, Davis, CA, United States

[3]UIH America, Inc., Houston, TX, United States

Abstract

Objective: This work assessed the relationship between image SNR and total-body noise-equivalent count rate (NECR) – for both non-TOF NECR and TOF-NECR – in a long uniform water cylinder and 14 healthy human subjects using the uEXPLORER total-body PET/CT scanner.

Approach: A TOF-NEC expression was modified for list-mode PET data, and both the non-TOF NECR and TOF-NECR were compared using datasets from a long uniform water cylinder and 14 human subjects scanned up to 12 hours after radiotracer injection.

Main results: The TOF-NECR for the uniform water cylinder was found to be linearly proportional to the TOF-reconstructed image SNR^2 in the range of radioactivity concentrations studied, but not for non-TOF NECR as indicated by the reduced R^2 value. The results suggest that the use of TOF-NECR to estimate the count rate performance of TOF-enabled PET systems may be more appropriate for predicting the SNR of TOF-reconstructed images.

Significance: Image quality in PET is commonly characterized by image signal-to-noise ratio (SNR) and, correspondingly, the noise-equivalent count rate (NECR). While the use of NECR for predicting image quality in conventional PET systems is well-studied, the relationship between SNR and NECR has not been examined in detail in long axial field-of-view total-body PET systems, especially for human subjects. Furthermore, the current NEMA NU 2-2018 standard does not account for count rate performance gains due to time-of-flight (TOF) in the NECR evaluation. The relationship between image SNR and total-body NECR in long axial FOV PET was assessed for the first time using the uEXPLORER total-body PET/CT scanner.

Disclosure

UC Davis has a research agreement and a sales-based revenue sharing agreement with United Imaging Healthcare. Ramsey D. Badawi and Simon R. Cherry are principal investigators on a research grant funded by United Imaging Healthcare.

Introduction

In positron emission tomography (PET), the image signal-to-noise ratio (SNR) is a common metric used to characterize image quality. A way to predict image SNR is to assess the count rate performance of a PET system by using the noise-equivalent count rate (NECR), a metric adopted into the National Electrical Manufacturers Association (NEMA) NU 2 standard (NEMA NU 2-2018), which estimates the effective true count rate of a PET system in the presence of scattered and random coincidences. The linear relationship between image SNR^2 and noise-equivalent count (NEC) was first introduced for linear reconstruction algorithms, such as filtered back-projection (FBP) (Brownell 1979 and Strother 1990). Later, it was shown that the relationship also applied experimentally for non-linear reconstruction methods, such as ordered-subset expectation-maximization (OSEM) algorithms (Dahlbom 2005). Based on this relationship, NECR can be used to optimize injected radiotracer dose, guide imaging protocol design, and can, in appropriate circumstances, directly predict image quality in humans (Lartizien 2002, Watson 2005, Danna 2006, Chang 2011, Carlier 2014).

For the first time, with long axial field-of-view (FOV) PET systems, such as the 194-cm uEXPLORER total-body PET/CT scanner, the entire adult human can be enclosed inside the scanner (Badawi 2019, Spencer 2021). The 15 – 68 fold increase in system sensitivity (Spencer 2021) across the adult human compared to conventional PET systems with 15 – 30 cm axial FOV widens the dynamic range of activity levels accessible to PET and enables, for example, delayed time point imaging, or imaging with reduced injected radioactivity (Badawi 2019, Berg 2020, Vera 2020, Liu 2021). The total-body scanner also enabled new research applications, such as dynamic imaging with sub-second frame lengths (Zhang 2020a), and kinetic modeling across the entire human body (Feng 2021, Wang 2021, Zhang 2020b).

The use of NECR as a surrogate metric to predict image quality in conventional PET systems is well-studied and is mathematically well-modeled in phantoms. At the same time, the relationship between image SNR and NECR has not yet been examined in human subjects when extended to a long axial FOV environment. With a 194-cm axial FOV and wide axial acceptance angles (at up to 57.0°) (Spencer 2021), the count rates across the uEXPLORER scanner can vary substantially in human subjects, especially during the early phase of dynamic imaging, which may not be well represented by phantom NECR experiments alone. When using conventional PET systems, it has also been suggested that the patient-specific NECR can vary across different bed positions (Watson 2005). As a result, the optimal injected dose may vary for different bed positions. With the uEXPLORER total-body scanner, a global NECR across the body (i.e. total-body NECR) can be obtained in a single bed position, which may help reduce complexity when developing imaging protocols and optimizing injected radioactivity based on a global metric independent of bed position. Another potential benefit when imaging the entire human body simultaneously is that the total radioactivity inside the human subject can be obtained using reconstructed images, even if voiding occurred between consecutive scans. This means that a global NECR curve across the entire human body can be produced using experimental data for the first time. This contrasts with conventional PET systems, where direct measurements

of the excretion are required to estimate the total radioactivity inside the subject, and tracer redistribution over the course of the scan is a potential confounder.

An important consideration when assessing NECR in total-body PET is that the NEMA NU 2 NECR protocol (NEMA NU 2-2018) does not account for count rate performance gains due to time-of-flight (TOF). Larger axial acceptance angles, combined with an order of magnitude greater volume of scintillator material than conventional scanners (Jakoby 2011, Spencer 2021), can lead to a large increase in the random coincidence count rate in the uEXPLORER scanner. As a result, TOF-NECR may be an important metric to assess the count rate performance of total-body PET scanners more appropriately. Non-TOF NECR only captures the sensitivity of a scanner to coincidence events and not the count rate dependent performance gain due to TOF. Previously, it was suggested that a TOF-enabled PET system improves image SNR due to the ability to better localize the site of annihilation along the line-of-response (LOR) and therefore reduces the variance in the reconstructed images (Snyder 1981, Budinger 1983, Moses 2003). There should be value in using TOF-NECR rather than non-TOF NECR as a surrogate metric to predict TOF-reconstructed image quality. Another consideration when assessing TOF-NECR is that the existing TOF-NECR expression (Conti 2006) was not directly implemented for list-mode PET data. A modification of the expression can be beneficial to better account for the geometry of the scanned objects and the system configuration of the uEXPLORER scanner.

Following the count rate performance and quantitative accuracy results measured previously in total-body PET (Spencer 2021, Leung 2021a), this work assessed the total-body NECR in a long uniform water cylinder and 14 healthy human subjects using the uEXPLORER scanner. To do so, the NEMA NU 2-2018 NECR expression as well as the TOF-NECR expression (Conti 2006) were modified to enable the processing of list-mode PET data. Then, the image SNR^2, non-TOF NECR, and TOF-NECR of the long uniform water cylinder and human subjects were assessed. The subjects were grouped according to body mass index (BMI) (normal weight = 18.5 – 24.9 kg/m^2, overweight = 25 – 29.9 kg/m^2, and obesity = 30 kg/m^2 and greater) to assess the effects of body habitus on the relationships between SNR and NECR. Finally, the relationship between optimal injected radioactivity concentration vs. BMI were examined, using a specified target TOF-NECR.

Methods

Derivation of NEC expressions for list-mode PET data

The SNR^2 expressions for both non-TOF and TOF were written in the following non-TOF and TOF forms for NEC, as shown in $NEC_{non-TOF} = \frac{T^2}{\left(T + S + \frac{D}{D_{FOV}}R\right)}$ (Equation 1 and 2 (Conti 2006):

$$NEC_{non-TOF} = \frac{T^2}{\left(T + S + \frac{D}{D_{FOV}}R\right)} \quad \text{(Equation 1)}$$

$$NEC_{TOF} = \frac{D}{\Delta x} \cdot \frac{T^2}{\left(T + S + \left(\frac{D}{D_{FOV}}\right)^2 R\right)} \quad \text{(Equation 2)}$$

Where T, S, and R are the true, scattered, and random coincidence counts, respectively; D is the object diameter; $D_{FOV} = ct_w/2$ is the diameter of the FOV, which depends on the speed of light c and the coincidence time window t_w; and $\Delta x = c\Delta t/2$ is the TOF localization uncertainty, which depends on the timing resolution of the PET system (Δt).

Then, $NEC_{non-TOF} = \frac{T^2}{\left(T + S + \frac{D}{D_{FOV}} R\right)}$ (Equation 1 and 2 were rewritten into NE

$C_{non-TOF} = \frac{(\sum_i T_i)^2}{\sum_i T_i + \sum_i S_i + \sum_i \left(\frac{D_i}{D_{FOV,i}} R_i\right)}$ (Equation 3 and 4 for list-mode coincidence data

over all LORs (Poon 2013):

$$NEC_{non-TOF} = \frac{(\sum_i T_i)^2}{\sum_i T_i + \sum_i S_i + \sum_i \left(\frac{D_i}{D_{FOV,i}} R_i\right)} \quad \text{(Equation 3)}$$

$$NEC_{TOF} = \frac{1}{\Delta x} \cdot \frac{(\sum_i D_i T_i)^2}{\sum_i D_i T_i + \sum_i D_i S_i + \sum_i \left(\frac{D_i^3}{D_{FOV,i}^2}\right) R_i} \quad \text{(Equation 4)}$$

where i is the ith LOR, $D_i = \max(D'_i \Delta x)$, where D'_i is the intersection distance between the ith LOR and the object; T_i, S_i, and R_i are the true, scattered, and random coincidence counts in the ith LOR, respectively; and $D_{FOV,i}$ is the diameter of the FOV for the ith LOR.

The randoms component in $NEC_{non-TOF} = \frac{T^2}{\left(T + S + \frac{D}{D_{FOV}} R\right)}$ (Equation 1 and 3 differs

from the NECR expression described in the NEMA NU 2-2018 NECR protocol by a factor of D/D_{FOV}. This is because in the protocol, the LORs that do not intersect the phantom are discarded. For consistency with the NU 2 NECR expression, Equations 3 and 4 were modified to reduce the randoms component by a factor of $D_i/D_{FOV,i}$, ultimately leading to $NEC_{non-TOF} = \frac{(\sum_i T_i)^2}{\sum_i T_i + \sum_i S_i + \sum_i R_i}$.

(Equation 5 (Poon 2013) and 6:

$$NEC_{non-TOF} = \frac{(\sum_i T_i)^2}{\sum_i T_i + \sum_i S_i + \sum_i R_i} \quad \text{(Equation 5)}$$

$$NEC_{TOF} = \frac{1}{\Delta x} \cdot \frac{(\sum_i D_i T_i)^2}{\sum_i D_i T_i + \sum_i D_i S_i + \sum_i \left(\frac{D_i^2}{D_{FOV,i}}\right) R_i} \quad \text{(Equation 6)}$$

To maintain similarity with the numerator of the non-TOF NEC expression shown in $NEC_{non-TOF} = \frac{(\sum_i T_i)^2}{\sum_i T_i + \sum_i S_i + \sum_i R_i}$ (Equation 5, the TOF-NEC expression in $NEC_{TOF} = \frac{1}{\Delta x} \cdot \frac{(\sum_i D_i T_i)^2}{\sum_i D_i T_i + \sum_i D_i S_i + \sum_i \left(\frac{D_i^2}{D_{FOV,i}}\right) R_i}$. (Equation 6 was divided by D_i^2 in both the numerator and denominator and was rewritten into $NEC_{TOF} = \frac{(\sum_i T_i)^2}{\sum_i \frac{\Delta x}{D_i}[T_i + S_i + \left(\frac{D_i}{D_{FOV,i}}\right) R_i]}$ (Equation 7:

$$NEC_{TOF} = \frac{(\sum_i T_i)^2}{\sum_i \frac{\Delta x}{D_i}[T_i + S_i + \left(\frac{D_i}{D_{FOV,i}}\right) R_i]} \quad \text{(Equation 7)}$$

where $\frac{\Delta x}{D_i} T_i$, $\frac{\Delta x}{D_i} S_i$, and $\frac{\Delta x}{D_{FOV,i}} R_i$ are the reduced variance of true, scattered, and random coincidence counts in the ith LOR, respectively. The expression in $NEC_{TOF} = \frac{(\sum_i T_i)^2}{\sum_i \frac{\Delta x}{D_i}[T_i + S_i + \left(\frac{D_i}{D_{FOV,i}}\right) R_i]}$ (Equation 7) shows that the reduced variance of the ith LOR is dependent of the timing resolution of the PET system (which is related to Δx), the object size (D_i), and the coincidence time window (which is related to $D_{FOV,i}$).

System parameters

The 194 cm long uEXPLORER scanner consists of 8 PET scanner units, with a 786 mm ring diameter. Each unit contains 24 detector modules, with each module containing 5 x 14 (transaxial x axial) detector blocks. Each block contains 7 x 6 (transaxial x axial) scintillator crystals (each 2.76 x 2.76 x 18.1 mm^3). The TOF resolution of the system is 505 ps, and the spatial resolution of the system is ≤ 3.0 mm full width at half maximum (FWHM) near the center of the scanner. The system utilizes a scanner unit-based variable time window (4.5 – 6.9 ns) and allows each unit to form coincidence events with up to a maximum unit difference of 4, corresponding to a maximum axial acceptance angle of 57.0°. The energy window of the system is 430 – 645 keV. Detailed information regarding the scanner is available in Spencer 2021.

Uniform phantom

An acrylic uniform water cylinder (16.5 cm outer diameter, 15 cm inner diameter, 210 cm long) filled with ^{18}F-FDG was positioned at the center of the scanner. List-mode PET data were acquired at five time points over 10 h, from 474 MBq to 17 MBq in the FOV of the scanner. Each scan was 60 min long, and twelve, 5 min long dynamic PET images were reconstructed. For consistency with our previous work (Leung 2021a), the same set of images were analyzed here. To assess the image SNR, 50 mm diameter spherical volumes of interest (VOIs) were drawn at the center of the FOV of the scanner and were analyzed using $SNR = \frac{\mu}{\sigma}$ (Equation 8:

$$SNR = \frac{\mu}{\sigma} \quad \text{(Equation 8)}$$

where μ and σ are the mean and standard deviation of the VOIs, respectively.

Human subjects

The study was conducted under an IRB-approved protocol (IRB #1341792) and all subjects gave written informed consent. Data from 14 healthy human subjects, all injected with ^{18}F-FDG, were selected for this work. Demographic characteristics of the subjects are shown in Table 1. The subjects were positioned at the center of the scanner in a supine position with their hands placed above the head at 90 min, 3 h, 6 h, 9 h, and 12 h after radiotracer injection and were scanned for 20 min at each time point. A 20 min per PET acquisition protocol was used in this work because our IRB-approved protocol was designed to maximize the quality of the PET images, and the acquisition duration was chosen to be in line with the existing clinical protocols for conventional PET scanners at our institution. The 20 min scan duration also provides us the ability to, in the future, explore shortening that duration further, for example via sub-sampling of the 20 min list-mode data, and documenting tradeoffs of the shorter acquisitions against the 20 min acquisition. A low-dose CT scan was performed at the 90 min time point (at 140 kVp, 50 mAs with dose modulation), while ultralow-dose CT scans were performed at the later time points (at 140 kVp, 5 – 20 mAs with dose modulation). The purpose of the low-dose CT scan at the 90 min time point was to obtain higher quality CT images than the ultra-low dose CT images while taking the overall CT dose given to the human subjects in this IRB-approved study into account.

The image SNR was assessed using a 50 mm diameter spherical VOI positioned in a uniform region of the liver. For human subjects with liver artifacts from significant respiratory motion, elongated cylindrical VOIs with similar number of voxels as the spherical VOIs were used instead. To account for activity redistribution in the liver as well as the variations in liver uptake across human subjects, the SNR^2 of the liver for time point t (SNR_t^2) was adjusted and normalized to the study population ($SNR_{adjusted,t}^2$) using $SNR_{adjusted,t}^2 = SNR_t^2 \times \frac{\overline{SUV_0}}{\frac{TIDA_0 \times 0.5^{t/T_{1/2}}}{TIDA_t} \times SUV_t}$ (Equation 9, with the assumption that the SNR can be scaled in a Poisson-like manner with radioactivity concentration for human subjects:

$$SNR^2_{adjusted,t} = SNR^2_t \times \frac{\overline{SUV}_0}{\frac{TIDA_0 \times 0.5^{t/T_{1/2}}}{TIDA_t} \times SUV_t} \quad \text{(Equation 9)}$$

where $\overline{SUV}_0$ is the averaged mean SUV of the liver from the 90 min scan across all subjects; $TIDA_0 \times 0.5^{t/T_{1/2}}$ is the expected total image-derived activity (TIDA) at time t after the 90 min scan, based on the TIDA from the 90 min scan ($TIDA_0$) and the half-life of ^{18}F ($T_{1/2}$ = 109.771 min); $TIDA_t$ is the TIDA at time t; and SUV_t is the mean SUV of the liver at time t.

Data processing

The non-TOF NECR and TOF-NECR were calculated using Equations 5 and 6 and divided by the acquisition length. Due to the large number (9.2 x 10^{10}) of LORs of the uEXPLORER scanner (Spencer 2021), the list-mode data were re-binned into detector block-pair sinograms to facilitate computational efficiency. True coincidences were estimated based on the subtraction of scattered and random coincidences from the prompt coincidence data. The scatter component in our NECR calculations, however, cannot be directly measured by the PET system and we therefore opted to estimate the scatter component using Monte Carlo simulations. As an effort to improve the inherent material limitations of typical Monte Carlo simulations, we have implemented a variable attenuation coefficient framework (Leung 2021b) into a customized version of the SimSET Monte Carlo simulation package (v2.9.2) (Harrison 1993). Each detector block-pair true plus scattered coincidence sinogram from the simulation was scaled to match the experimental prompt minus delay detector block-pair sinogram using least squares fitting. The variable attenuation coefficients method for scatter estimation is described in the Appendix. Finally, random coincidences were obtained from the delayed coincidence channel.

For consistency with the NEMA NU 2-2018 NECR protocol, coincidence events outside the scanned object were excluded. To do so, the bed in the CT image volume was first removed using an automated segmentation method based on a VOI of the scanner bed. Then, a binary mask based on the thresholded forward projection of the CT image volume (to exclude air) was applied to the detector block-pair sinograms.

Image reconstruction

The PET images were reconstructed using a research-only list-mode TOF-OSEM reconstruction platform provided by the vendor and installed on in-house computational hardware. For consistency with our previous work on assessing the quantification accuracy of the uEXPLORER scanner (Leung 2021a), all images were reconstructed with 4 iterations, 20 subsets, and with 4 mm isotropic voxels in a 150 x 150 x 486 image matrix. Resolution modeling (i.e. point spread function (PSF)) was not included, and post-reconstruction smoothing was not applied to the reconstructed images. All other PET data corrections were applied, including corrections for scattered and random coincidences, attenuation, dead-time, normalization, and radioactive decay.

Results

Uniform phantom

The non-TOF NECR and TOF-NECR of the uniform phantom are shown in Figure 1. At a radioactivity concentration of ~14 kBq/mL, the TOF-NECR was 3.1-fold higher than non-TOF NECR. Also, while the non-TOF NECR curve began to plateau as the radioactivity concentration approached 15 kBq/mL, the TOF-NECR curve continued to increase. Figure 2 shows the relationships between SNR^2 and non-TOF NECR, as well as TOF-NECR, respectively. The relationship between SNR^2 and non-TOF NECR was initially linear, however the SNR^2 increased more rapidly than non-TOF NECR at higher count rates (as a reminder the non-TOF NECR vs. activity concentration curve began to plateau at 3000 kcps), while the relationship between SNR^2 and TOF-NECR was linear over the range of values studied. The R^2 fits for SNR^2 vs. non-TOF NECR and TOF-NECR were 0.94 and 0.98, respectively.

Human subjects

Figure 3 shows the non-TOF NECR and TOF-NECR of the human subjects, plotted against the activity concentration. Figure 4 shows the relationship between the adjusted SNR^2 and non-TOF NECR, as well as TOF-NECR, respectively. To assess the linearity of the results, a linear fit was performed individually on each human subject since the slope of the SNR^2 vs. non-TOF NECR and TOF-NECR depends on the geometry as well as the activity distribution of the scanned object. The mean R^2 values for the adjusted SNR^2 vs. non-TOF NECR and TOF-NECR of all 14 human subjects were 0.98±0.03 and 0.98±0.02, respectively. Figure 5 shows the adjusted SNR^2 of the study population, plotted against non-TOF NECR, and TOF-NECR. The R^2 fits for the adjusted SNR^2 vs. non-TOF NECR and TOF-NECR were 0.91 and 0.88, respectively. Also, based on the results, we determined if a specific injected radioactivity concentration can be found for a given TOF-NECR with respect to BMI. Figure 6. The optimal radioactivity concentration vs. BMI when TOF-NECR = 3000 kcps for the 14 human subjects.6 shows the optimal radioactivity concentration vs. BMI when a target TOF-NECR of 3000 kcps was specified, which was chosen since it approximates the average TOF-NECR expected from the clinical imaging protocol implemented at our facility (Nardo 2021). The R^2 value for the plot was 0.87.

Discussion

The NECR results shown in Figure 1 cover the radioactivity concentration range for typical uEXPLORER ^{18}F-FDG PET scans (~300 MBq injected, with the scan beginning at 120 min after radiotracer injection), which may suggest that for this scanner, the injected radioactivity in human subjects may be increased beyond the radioactivity concentration at peak non-TOF NECR (if permitted) to improve TOF-reconstructed image SNR. The non-TOF NECR results suggested a radioactivity concentration of approximately 15 kBq/mL at peak non-TOF NECR, with diminishing gains starting at approximately 10 kBq/mL. The TOF-NECR results, on the other hand, continued to increase more strongly than the non-TOF NECR results, suggesting that the radioactivity concentration at peak TOF-NECR may be substantially higher than that at peak non-TOF NECR. Furthermore, the

TOF-NECR results in Figure 2 were linearly correlated with image SNR^2, while the image SNR^2 increased more rapidly than the linear fit at higher non-TOF NECR where it began plateauing in Figure 1, suggesting that the TOF-NECR metric may be more suitable for directly predicting the image quality of the uEXPLORER scanner. Given that TOF-enabled PET systems are expected to improve image SNR (Snyder 1981, Budinger 1983, Moses 2003), the results may also suggest the radioactivity concentration limits expected from the standard non-TOF NECR measurements may be less appropriate for estimating the effective count rate performance of the TOF-enabled uEXPLORER total-body scanner. This may especially be an important consideration when imaging radiotracers with shorter half-lives, such as in ^{82}Rb cardiac imaging ($T_{1/2}$ = 76.38 s) or in ^{15}O studies ($T_{1/2}$ = 122.24 s), though further investigation by assessing image SNR for these imaging scenarios is needed. Overall, it was found that the relationship between image SNR^2 and non-TOF NECR may not always be linear for images reconstructed with the TOF-OSEM algorithm, which suggests that the use of TOF-NECR may be more appropriate for assessing the count rate performance of PET systems with TOF capabilities.

In Figure 3, the non-TOF NECR curves for all 14 human subjects overlapped with each other when plotted against radioactivity concentration, but not for TOF-NECR. In addition, the TOF-NECR curves showed higher NECR at a given radioactivity concentration with higher BMIs. We suggest that this may be related to the combination of higher total radioactivity in the higher BMI subjects (for a given radioactivity concentration) during the scan as well as the greater count rate performance gains due to TOF for larger subjects (as depicted by the object size D_i in Equation 7). The overlaps between human subjects across BMIs with non-TOF NECR is peculiar and suggests that a weight-based dosing scheme may potentially be appropriate for adult humans when assessing non-TOF reconstructed images from the uEXPLORER scanner, although further investigation is needed.

In Figure 4, the image SNR^2 vs. non-TOF NECR overlapped between subjects across a wide range of BMIs, but less so for TOF-NECR. While this may be related to the effects of BMI on TOF-NECR, the variations in activity distribution between different subjects can affect the NECR curves and subsequently the slope of the SNR^2 vs. NECR plots. At the same time, the activity range assessed in the human subjects did not approach peak non-TOF NECR and may explain the similar R^2 values observed for image SNR^2 vs. non-TOF NECR and TOF-NECR in both Figures 4 and 5. Future studies that utilize phantoms with varying diameters and lengths, as well as increasing the activity level in humans (if permitted), may provide more insight on this.

In Figure 6, the optimal activity concentration decreased with BMI for a given TOF-NECR. While this may be unexpected at first glance, the injected activity for a given TOF-NECR in our data increased with BMI, in agreement with the literature (Xiao 2021).

Overall, although a linear relationship was found between SNR^2 of OSEM-reconstructed images and TOF-NECR for both the uniform water phantom and human subjects, caution should be exercised to not overinterpret the data for several reasons: while it was previously reported (Dahlbom 2005) that the non-TOF reconstructed image SNR^2 and non-TOF NECR were linearly proportional to each other using OSEM reconstructions (up to 120 kcps) and

that similar trends were found in some of this work with TOF reconstructions, the OSEM algorithm itself is not a linear reconstruction algorithm, and therefore the results may vary significantly depending on the reconstruction parameters. Also, at low count conditions some of the additional non-linear behavior between image SNR^2 and TOF-NECR may be related to the non-negativity constraints imposed by Poisson distribution. Additional work using a variety of reconstruction parameters, such as using different reconstruction voxel sizes and varying number of subsets and iterations to ensure convergence, is needed to ensure the linear relationship applies for a wide variety of imaging conditions. Also, for the human subject studies, despite the ability to derive the total radioactivity in the human subjects based on reconstructed images, we do not have an independent measure of radioactivity (e.g., from the dose calibrator), since the subjects voided between consecutive scans. It may be beneficial to collect and measure the amount of radioactivity in the excretion between scans to ensure all radioactivity is directly measured and accounted for. Finally, both the image SNR in the liver and the NECR can vary since ^{18}F-FDG redistributes in the body over time. Additional work using other tracers that are more stable in the liver and/or other organs over longer durations, such as ^{68}Ga-NEB, which binds to serum albumin (Niu 2014, Zhang 2015), and re-sampling (bootstrap) of list-mode data to generate multiple realizations to exclude the population variance, may further strengthen the robustness of total-body TOF-NECR estimation in humans.

Conclusion

The relationship between image SNR and total-body NECR in long axial FOV PET was assessed for the first time using the uEXPLORER total-body PET/CT scanner. The TOF-NEC expression (Conti 2006) was modified for list-mode PET data, and both the non-TOF NECR and TOF-NECR were compared using datasets from a long uniform water cylinder and 14 human subjects scanned up to 12 hours after radiotracer injection. The TOF-NECR for the uniform water cylinder was found to be linearly proportional to the TOF-reconstructed image SNR^2 in the range of radioactivity concentrations studied, but not for non-TOF NECR as indicated by the reduced R^2 value. In this work, we showed that the use of TOF-NECR to estimate the count rate performance of TOF-enabled PET systems was more appropriate for predicting the SNR of TOF-reconstructed images in phantoms. Peculiarly, the non-TOF NECR curves for all 14 human subjects overlapped with each other when plotted against radioactivity concentration, but not for TOF-NECR, suggesting a weight-based dosing scheme may potentially be appropriate for adult humans when assessing non-TOF reconstructed images from the uEXPLORER scanner. Additional phantom and human studies are needed to further establish the applicability of TOF-NECR in PET systems with TOF capabilities.

Acknowledgement

We thank Dr. Robert L. Harrison for his help in modifying the SimSET source code to accept additional material definitions. We also thank Dr. Jonathan K. Poon for his initial work on deriving the non-TOF NECR and TOF-NECR expressions for list-mode PET data. Finally, we thank Dr. Terry Jones for his valuable discussions which helped refine this work. Funding sources for this work include NIH R01 CA206187 and NIH R01 CA249422.

Appendix

To perform Monte Carlo scatter estimation, the required components are: 1) an attenuation map, in the form of a material map; 2) an activity map; 3) a model of the scanner and its electronics; and 4) a Monte Carlo physics engine. With experimental images as the input, the material map is typically generated via a threshold-based segmentation of the CT image volume. Due to the limited number of materials available in common Monte Carlo simulation software, such as GATE (Jan 2004) and SimSET (Harrison 1993), the attenuation map is typically segmented into only a few materials (Levin 1995, Moliner 2019). As shown in Figure A1, the Hounsfield Unit (HU) distribution in a healthy adult human is continuous and is therefore may not be well represented by only a very small number of materials. When the granularity of the material map is limited, the accuracy of scatter estimation may be affected, particularly in regions where the attenuation and scattering properties vary widely, such as in the thorax region which includes the lung, heart, and bone tissues.

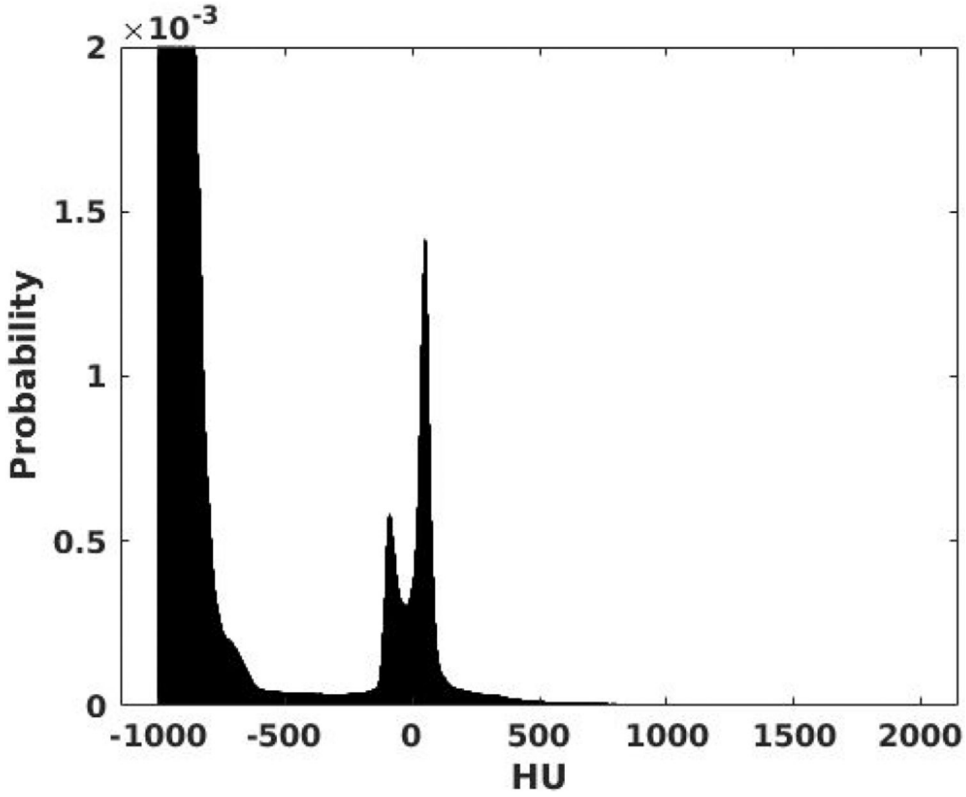

Figure A1.
HU probability distribution in the CT image volume of a representative healthy adult human subject scanned using the uEXPLORER scanner.

To preserve the granularity of the attenuation map (converted from the CT image volume) used in the simulation, a method that generates a continuous water density map from the CT image volume was developed, which serves as a surrogate to the material map required for the simulations. The method was validated against default SimSET materials using both count statistics and reconstructed images from an XCAT phantom and evaluated in

the projection space to eliminate influences due to image reconstruction, using a custom phantom constructed from a 3 x 3 grid of square tubing (not shown). The SimSET source code was modified to increase the maximum number of materials from 100 (29 standard materials + 71 placeholder materials) to 22100 materials (100 default SimSET materials + 22000 water density materials). The water density materials corresponded to water densities ranging from 0.001 g/cm^3 to 2.2 g/cm^3 (in 0.001 g/cm^3 increments) and were generated using the SimSET material generator. The water density range covers a wide range of Hounsfield Units (HUs) expected in the CT image volume of a healthy adult human subject, as shown in Figure A1.

The material index map for SimSET was generated using a 3-part process as shown in FigureA2. The DICOM CT image volume was read, then rescaled with the associated rescale slope and intercept. The CT images were then interpolated and resized as needed to match the dimensions of the activity map. The voxel values in the CT images were limited to between −1000 HU and 2000 HU to remove outlier values introduced by potential image artifacts, as well as to reduce the number of materials required to encompass the specified HU range, which minimized the initialization time required for the simulation (it takes approximately an hour to load 20000+ material definitions into SimSET). As shown earlier in Figure A1, the CT HU distribution of human subjects scanned using the uEXPLORER scanner demonstrated that a 2000 HU upper limit was sufficient to cover the entire range of HU units in healthy humans, though the lower and upper limits can be tailored for each human subject (e.g., to account for metal implants) if needed. Next, the 511-keV attenuation map was generated using bilinear fitting, as shown in Below break point: $\mu = 9.6 \times 10^{-5}$ ■ $(HU + 1000)$ cm^{-1} (EquationA1 and Above break point: $\mu = a \cdot (HU + 1000) + b$ cm^{-1} (EquationA2 (Carney 2006):

$$\text{Below break point: } \mu = 9.6 \times 10^{-5} \cdot (HU + 1000)\,\text{cm}^{-1} \qquad \text{(Equation A1)}$$

$$\text{Above break point: } \mu = a \cdot (HU + 1000) + b\,\text{cm}^{-1} \qquad \text{(Equation A2)}$$

where μ is the 511-keV linear attenuation coefficient (in cm^{-1}), and HU, a, and b are the X-ray tube kVp-dependent values (Carney 2006).

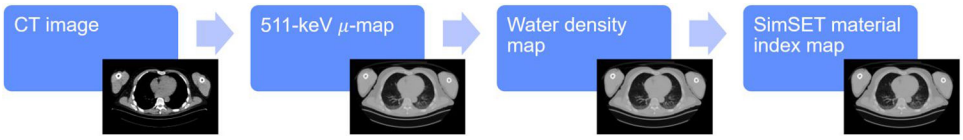

Figure A2.
A general overview of converting a CT image into a SimSET material index map.

Once the 511-keV attenuation map was generated, each voxel value in the attenuation map was fitted to an associated water density (0.0001 g/cm^3 increments) that had the closest corresponding 511-keV attenuation coefficient. Preliminary analysis suggested that an appropriate water density material may be used as a surrogate to replace the default SimSET materials used for the XCAT phantom. Figure A3 shows agreement (substantially

less than 1% difference) between the linear attenuation coefficient vs. photon energy plots of the brain, bone, and respective fitted water density materials between 430 keV (the LLD of the uEXPLORER scanner) and 511 keV. For the default SimSET bone material, the difference at 200 keV was 2.5%. Finally, the water density map was converted into the SimSET material index map for the simulation and an index translator was used to convert the material index map into materials defined in the customized SimSET software.

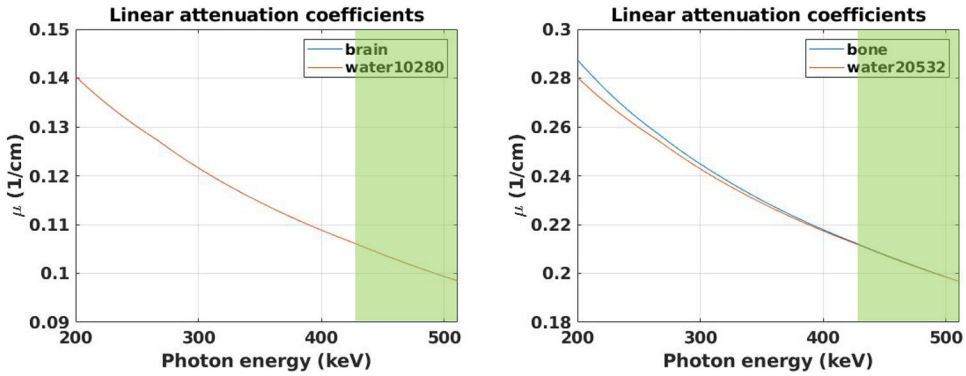

Figure A3.

The linear attenuation coefficient vs. photon energy plots for the (Left) SimSET brain material, and (Right) SimSET bone material, with respective fitted water density materials. The region highlighted in green shows the energy range between the LLD of the uEXPLORER scanner (430 keV) and 511 keV.

References

Badawi RD, Shi H, Hu P, Chen S, Xu T, Price PM, Ding Y, Spencer BA, Nardo L, Liu W, Bao J, Jones T, Li H and Cherry SR 2019 First Human Imaging Studies with the EXPLORER Total-Body PET Scanner The Journal of nuclear medicine 60 299–303 [PubMed: 30733314]

Berg E, Gill H, Marik J, Ogasawara A, Williams S, van Dongen G, Vugts D, Cherry SR and Tarantal AF 2020 Total-Body PET and Highly Stable Chelators Together Enable Meaningful 89Zr-Antibody PET Studies up to 30 Days After Injection The Journal of nuclear medicine 61 453–60 [PubMed: 31562219]

Brownell GL, Correia JA and Zamenhof RG 1979 "Positron Instrumentation" in Recent Advances in Nuclear Medicine (New York: Grune & Stratton)

Budinger TF 1983 Time-of-Flight Positron Emission Tomography: Status Relative to Conventional PET The Journal of nuclear medicine 24 73–8 [PubMed: 6336778]

Carlier T, Ferrer L, Necib H, Bodet-Milin C, Rousseau C and Kraeber-Bodéré F 2014 Clinical NECR in 18F-FDG PET scans: optimization of injected activity and variable acquisition time. Relationship with SNR Physics in medicine & biology 59 6417–30 [PubMed: 25295879]

Carney JPJ, Townsend DW, Rappoport V and Bendriem B 2006 Method for transforming CT images for attenuation correction in PET/CT imaging Medical physics (Lancaster) 33 976–83 [PubMed: 16696474]

Conti M 2006 Effect of randoms on signal-to-noise ratio in TOF PET IEEE transactions on nuclear science 53 1188–93

Chang T, Chang G, Kohlmyer S, Clark JW, Rohren E and Mawlawi OR 2011 Effects of injected dose, BMI and scanner type on NECR and image noise in PET imaging Physics in medicine & biology 56 5275–85 [PubMed: 21791730]

Dahlbom M, Schiepers C and Czernin J 2005 Comparison of noise equivalent count rates and image noise IEEE transactions on nuclear science 52 1386–90

Danna M, Lecchi M, Bettinardi V, Gilardi M, Stearns C, Lucignani G and Fazio F 2006 Generation of the Acquisition-Specific NEC (AS-NEC) Curves to Optimize the Injected Dose in 3D ^18F-FDG Whole Body PET Studies IEEE transactions on nuclear science 53 86–92

Feng T, Zhao Y, Shi H, Li H, Zhang X, Wang G, Price PM, Badawi RD, Cherry SR and Jones T 2021 Total-Body Quantitative Parametric Imaging of Early Kinetics of 18F-FDG Journal of Nuclear Medicine 62 738–44 [PubMed: 32948679]

Harrison RL, Vannoy SD, Haynor DR, Gillispie SB, Kaplan MS and Lewellen TK 1993 Preliminary experience with the photon history generator module of a public-domain simulation system for emission tomography Conf. Rec. IEEE Nucl. Sci. Symp 1154–1158

Jakoby BW, Bercier Y, Conti M, Casey ME, Bendriem B and Townsend DW 2011 Physical and clinical performance of the mCT time-of-flight PET/CT scanner Physics in medicine & biology 56 2375–89 [PubMed: 21427485]

Jan S, Santin G, Strul D, Staelens S, Assié K, Autret D, Avner S, Barbier R, Bardiès M, Bloomfield PM, Brasse D, Breton V, Bruyndonckx P, Buvat I, Chatziioannou AF, Choi Y, Chung YH, Comtat C, Donnarieix D, Ferrer L, Glick SJ, Groiselle CJ, Guez D, Honore PF, Kerhoas-Cavata S, Kirov AS, Kohli V, Koole M, Krieguer M, Laan D J v d, Lamare F, Largeron G, Lartizien C, Lazaro D, Maas MC, Maigne L, Mayet F, Melot F, Merheb C, Pennacchio E, Perez J, Pietrzyk U, Rannou FR, Rey M, Schaart DR, Schmidtlein CR, Simon L, Song TY, Vieira JM, Visvikis D, Walle R V d, Wieërs E and Morel C 2004 GATE: a simulation toolkit for PET and SPECT Physics in medicine & biology 49 4543–61 [PubMed: 15552416]

Lartizien C, Comtat C, Kinahan PE, Ferreira N, Bendriem B and Trebossen R 2002 Optimization of Injected Dose Based on Noise Equivalent Count Rates for 2- and 3-Dimensional Whole-Body PET The Journal of nuclear medicine 43 1268–78 [PubMed: 12215569]

Leung EK, Berg E, Omidvari N, Spencer BA, Li E, Abdelhafez YG, Schmall JP, Liu W, He L, Tang S, Liu Y, Dong Y, Jones T, Cherry SR and Badawi RD 2021a Quantitative accuracy in total-body imaging using the uEXPLORER PET/CT scanner Physics in medicine & biology 66

Leung E, Revilla E, Spencer B, Xie Z, Zhang X, Omidvari N, Badawi R, Cherry S, Lu Y and Berg E 2021b A quantitative image reconstruction platform with integrated motion detection for total-body PET. Soc Nuclear Med

Levin CS, Dahlbom M and Hoffman EJ 1995 A Monte Carlo correction for the effect of Compton scattering in 3-D PET brain imaging IEEE transactions on nuclear science 42 1181–5

Liu G, Hu P, Yu H, Tan H, Zhang Y, Yin H, Hu Y, Gu J and Shi H 2021 Ultra-low-activity total-body dynamic PET imaging allows equal performance to full-activity PET imaging for investigating kinetic metrics of 18 F-FDG in healthy volunteers European Journal of Nuclear Medicine and Molecular Imaging 1–11

Moliner L, Rodríguez-Alvarez MJ, Catret JV, González A, Ilisie V and Benlloch JM 2019 NEMA Performance Evaluation of CareMiBrain dedicated brain PET and Comparison with the whole-body and dedicated brain PET systems Scientific reports 9 15484–10 [PubMed: 31664096]

Moses WW 2003 Time of flight in PET revisited IEEE transactions on nuclear science 50 1325–30

Nardo L, Abdelhafez YG, Spencer BA and Badawi RD 2021 Clinical Implementation of Total-Body PET/CT at University of California, Davis PET Clinics 16(1) 1–7 [PubMed: 33218600]

NEMA Standards Publication NU 2-2018: Performance Measurements of Positron Emission Tomographs (PET) National Electrical Manufacturers Association (2018)

Niu G, Lang L, Kiesewetter DO, Ma Y, Sun Z, Guo N, Guo J, Wu C and Chen X 2014 In Vivo Labeling of Serum Albumin for PET The Journal of nuclear medicine 55 1150–6 [PubMed: 24842890]

Poon JK 2013 The performance limits of long axial field of view PET scanners (Davis, Calif: University of California, Davis)

Snyder DL, Thomas LJ and Ter-Pogossian MM 1981 A Matheematical Model for Positron-Emission Tomography Systems Having Time-of-Flight Measurements IEEE transactions on nuclear science 28 3575–83

Spencer BA, Berg E, Schmall JP, Omidvari N, Leung EK, Abdelhafez YG, Tang S, Deng Z, Dong Y, Lv Y, Bao J, Liu W, Li H, Jones T, Badawi RD and Cherry SR 2021 Performance Evaluation of the uEXPLORER Total-Body PET/CT Scanner Based on NEMA NU 2-2018 with Additional Tests

to Characterize PET Scanners with a Long Axial Field of View Journal of Nuclear Medicine 62 861–70 [PubMed: 33008932]

Strother SC, Casey ME and Hoffman EJ 1990 Measuring PET scanner sensitivity: relating countrates to image signal-to-noise ratios using noise equivalents counts IEEE transactions on nuclear science 37 783–8

Vera DB, Schulte B, Henrich T, Flavell R, Seo Y, Abdelhafez Y, Badawi R, Cherry S and VanBrocklin H 2020 First-in-human total-body PET imaging of HIV with 89Zr-VRC01 on the EXPLORER. Soc Nuclear Med

Wang G, Nardo L, Parikh M, Abdelhafez YG, Li E, Spencer BA, Qi J, Jones T, Cherry S and Badawi RD 2021 Total-Body PET Multiparametric Imaging of Cancer Using a Voxel-wise Strategy of Compartmental Modeling The Journal of nuclear medicine 10.2967/jnumed.121.262668

Watson CC, Casey ME, Bendriem B, Carney JP, Townsend DW, Eberl S, Meikle S and DiFilippo FP 2005 Optimizing Injected Dose in Clinical PET by Accurately Modeling the Counting-Rate Response Functions Specific to Individual Patient Scans The Journal of nuclear medicine 46 1825–34 [PubMed: 16269596]

Xiao J, Yu H, Sui X, Hu Y, Cao Y, Liu G, Zhang Y, Hu P, Wang Y, Li C, Xu B and Shi H 2021 Can the BMI-based dose regimen be used to reduce injection activity and to obtain a constant image quality in oncological patients by 18F-FDG total-body PET/CT imaging? European Journal of Nuclear Medicine and Molecular Imaging 49 269–278 [PubMed: 34185138]

Zhang J, Lang L, Zhu Z, Li F, Niu G and Chen X 2015 Clinical Translation of an Albumin-Binding PET Radiotracer 68Ga-NEB The Journal of nuclear medicine 56 1609–14 [PubMed: 26251416]

Zhang X, Cherry SR, Xie Z, Shi H, Badawi RD and Qi J 2020a Subsecond total-body imaging using ultrasensitive positron emission tomography Proceedings of the National Academy of Sciences - PNAS 117 2265–7

Zhang X, Xie Z, Berg E, Judenhofer MS, Liu W, Xu T, Ding Y, Lv Y, Dong Y, Deng Z, Tang S, Shi H, Hu P, Chen S, Bao J, Li H, Zhou J, Wang G, Cherry SR, Badawi RD and Qi J 2020b Total-Body Dynamic Reconstruction and Parametric Imaging on the uEXPLORER The Journal of nuclear medicine 61 285–91 [PubMed: 31302637]

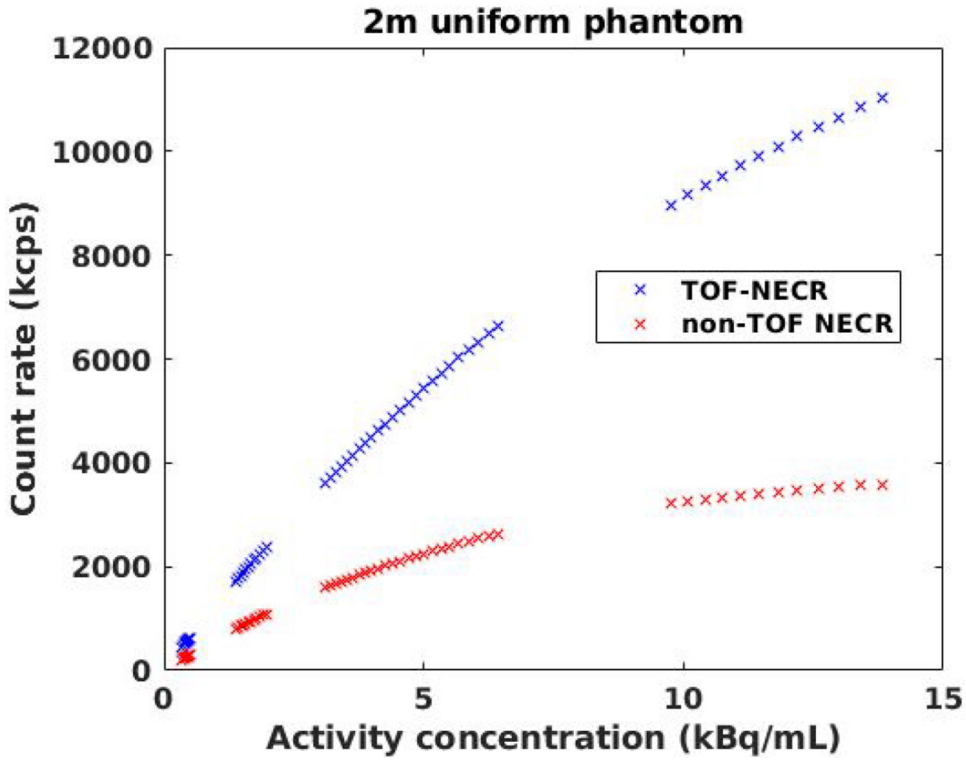

Figure 1.
The non-TOF NECR and TOF-NECR of the uniform phantom.

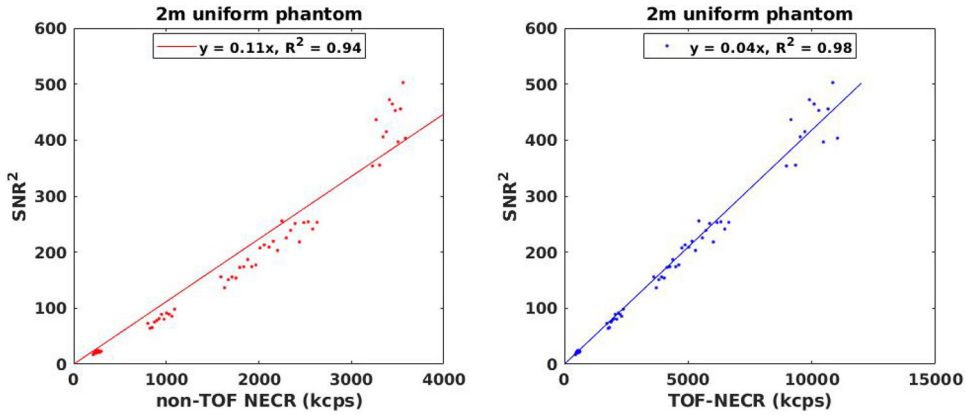

Figure 2.

The image SNR^2 of the uniform phantom, plotted against (left) non-TOF NECR (0 – 4000 kcps range), and (right) TOF-NECR (0 – 15000 kcps range).

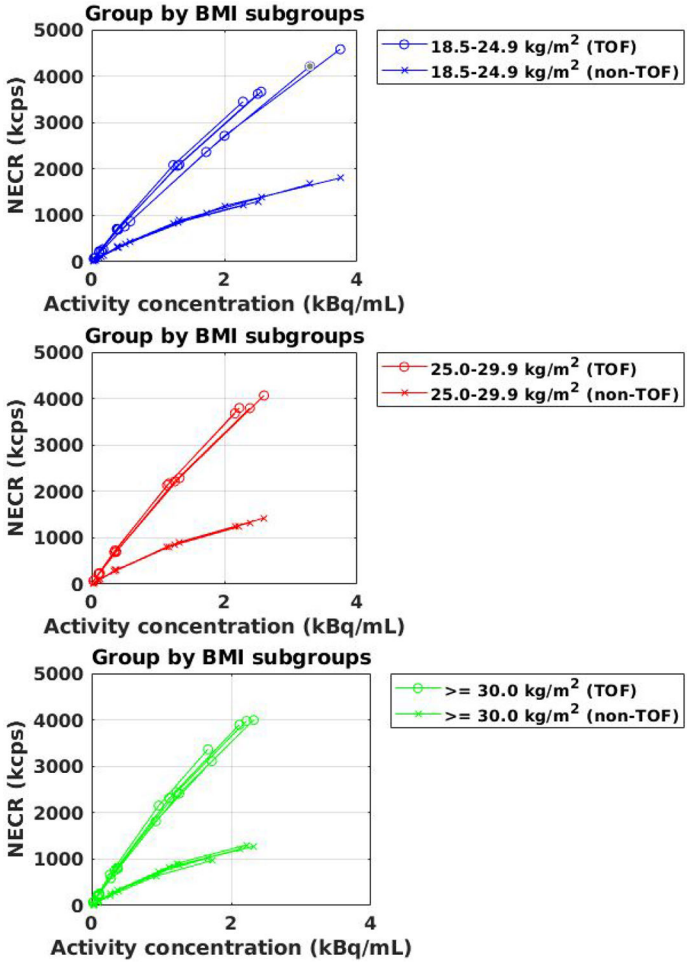

Figure 3.

The non-TOF NECR and TOF-NECR of human subjects, plotted against radioactivity concentration.

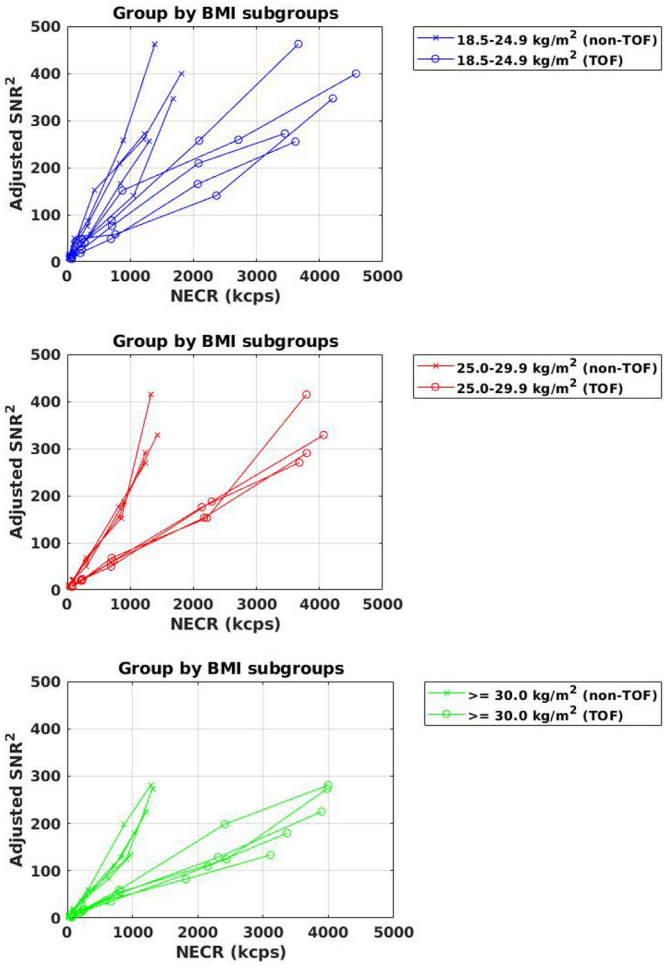

Figure 4.

The adjusted SNR^2 of the human subjects, plotted against non-TOF NECR and TOF-NECR. A linear fit was performed on each human subject, and the mean R^2 values for SNR^2 vs. non-TOF NECR and TOF-NECR of all 14 human subjects were 0.98±0.03 and 0.98±0.02, respectively.

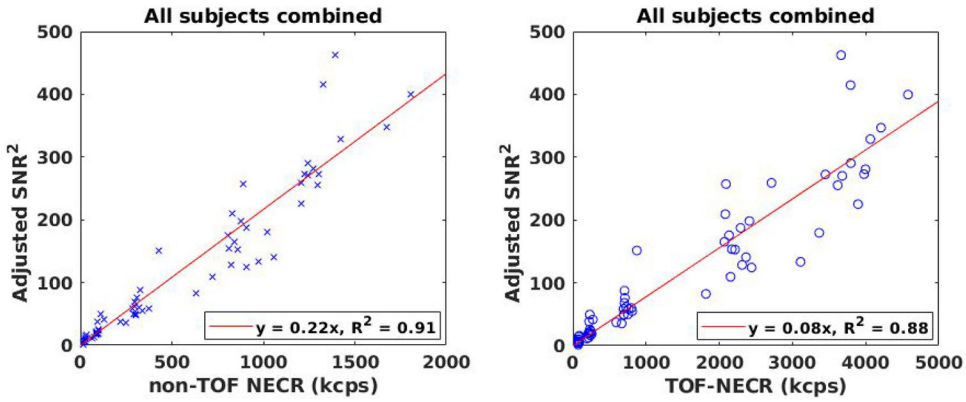

Figure 5.

The adjusted SNR^2 of the study population, plotted against (left) non-TOF NECR, and (right) TOF-NECR.

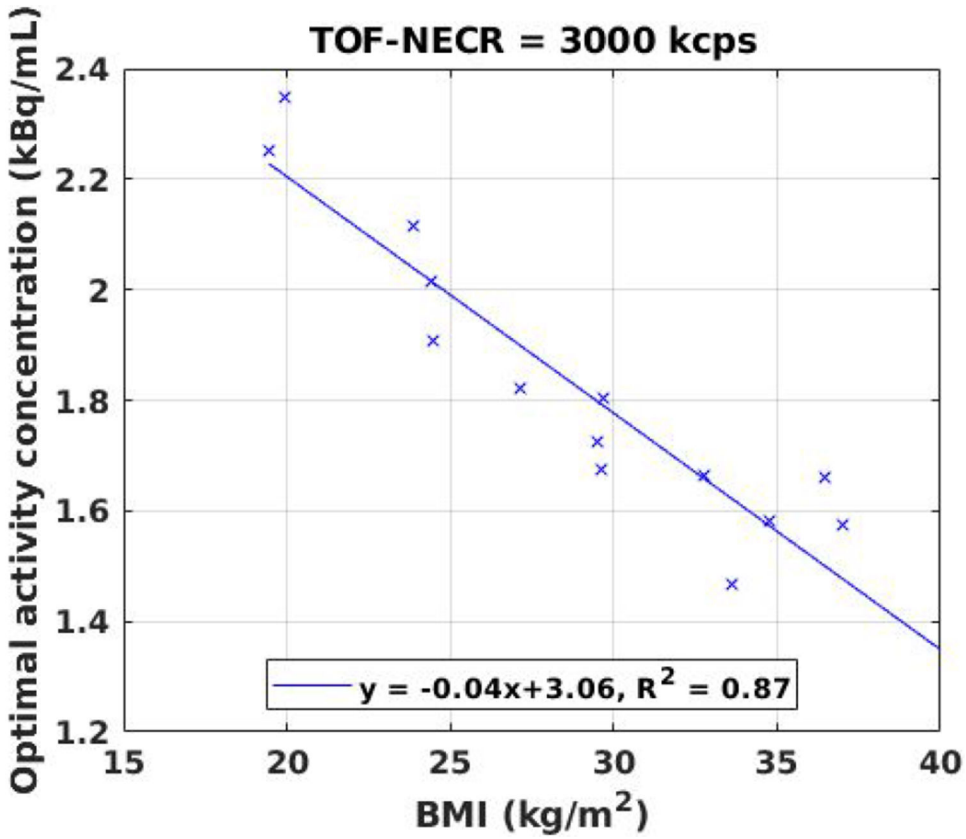

Figure 6.
The optimal radioactivity concentration vs. BMI when TOF-NECR = 3000 kcps for the 14 human subjects.

Table 1.

Demographic characteristics of the healthy human subjects (n=14).

Parameter	Value: min – max (mean±SD)
Age (years)	29 – 78 (50.6±13.4)
BMI (kg/m^2)	19.4 – 37.0 (28.8±5.8)
Weight (kg)	53.0 – 109 (80.0±15.5)
Height (m)	1.57 – 1.80 (1.67±0.07)
Injected ^{18}F-FDG activity (MBq)	337 – 394 (371±17)